Understanding the Mechanism of Nanocluster Formation from Machine-Learned Potential-based Simulations

Vikas Tiwari and Tarak Karmakar*

Department of Chemistry, Indian Institute of Technology, Delhi, 110016 New Delhi, India

E-mail: tkarmakar@chemistry.iitd.ac.in

Phone: +91 11 2654 8549

Abstract

Understanding the mechanism for the formation of metal nanoclusters is an open challenge in the nanoscience field. Computational modeling can provide molecular details of nanocluster formation that are otherwise inaccessible. However, even with advanced computational resources, simulating the nucleation of a nanocluster in solution presents significant challenges, including inaccurate energy predictions and limitations on system size and timescale. This work addresses these challenges by integrating deep neural networks (DNN) with well-tempered metadynamics (WT-Metad) to model the nucleation of an $Ag_6(SCNH_2)_6$ (a prototypical example) in solution. An unbiased neural network potential (NNP)–based molecular dynamics (MD) simulation captured the cluster's dynamic behavior, while WT-Metad simulations revealed an almost barrierless downhill transition from dispersed precursors to a nucleated state. Scaling up the system to 30 randomly distributed precursors demonstrated spontaneous nucleation at multiple sites, underscoring the method's robustness. This study presents the first successful DNN model of nanocluster formation in solution with DFT-level accuracy, paving the way for advancements in the field.

Atomically precise metal nanoclusters, comprising a small number of metal atoms, usually Au, Ag, or Cu, ranging from a few to several hundred, represent a unique class of materials between the atomic and nanoparticle scales.[1] These nanoclusters have a metal core with specific geometry protected by a monolayer of organic ligands stabilizing the core. Their small size and high surface-to-volume ratio imbue them with distinct physical and chemical properties, such as quantum size effects, unique optical characteristics, and enhanced catalytic activities.[2,3] These properties make nanoclusters highly significant for a wide range of applications, including catalysis,[4–6] energy storage,[7] energy conversion,[8,9] sensors,[10–12] and biomedical fields.[13–15] Designing nanoclusters for specific applications is a critical focus in this field, requiring a deep understanding of their formation and stabilization processes.[16,17] This knowledge is essential for tailoring nanocluster properties, such as size, shape, and composition, to meet the demands of various applications.[18] For instance, precise control over these attributes could lead to breakthroughs in developing more efficient catalysts or highly targeted drug delivery systems.[5,19] Thus, uncovering the mechanisms that govern nanocluster formation remains a vital and active area of research.[20–26]

The formation of nanoclusters in solution typically involves nucleation and growth processes, which are influenced by numerous factors such as temperature, concentration, and solvent interactions.[23] The nucleation stage is especially critical, as it determines the clusters' initial structural and energetic characteristics. Understanding the mechanism of nanocluster nucleation is therefore essential for controlling the synthesis process.[20] Furthermore, such insights enable the prediction and manipulation of nanocluster stability, morphology, and functionality, paving the way for more efficient material design.[27] Computational methods have proven to be invaluable tools for understanding nanoclusters at the molecular level.[28,29] However, despite their significance, modeling the nucleation of nanoclusters remains a challenging task.[30] Conventional computational methods, such as classical molecular dynamics (MD), cannot provide accurate results due to the lack of electronic degrees of freedom. More accurate *ab initio* MD methods suffer from timescales and length-scale limitations associated

with nucleation which are often beyond the reach of these methods and require significant computational resources. In addition, the free-energy landscape involved in nucleation is rugged and multidimensional, which hinders the accurate prediction of nucleation pathways and barriers.

Recently, machine learning-based methods have been employed to predict various properties and processes of nanoclusters, including their structure, stability, synthesis, small molecule adsorption, oxygen reduction, intercluster reactions, hydride locations, and force fields.[31–43] In a recent study by Häkkinen and coworkers,[42] the atomic cluster expansion (ACE) interatomic potential was employed to simulate the dynamics of gold nanoclusters in the gas phase. To the best of our knowledge, no studies to date have focused on modeling the formation and nucleation of nanoclusters in the solvent phase. In this work, we present a machine learning model designed to study the solvent-phase nucleation of metal nanoclusters using advanced approaches that integrate deep neural networks (DNN) with enhanced sampling techniques such as metadynamics (MetaD) and on-the-fly probability-enhanced sampling (OPES). These approaches have proven to be promising tools for understanding gas-phase heterogeneous catalytic systems as well as solution-phase modeling of complex chemical reactions.[44–49] Neural network potentials (NNP) have emerged as powerful models to accurately describe complex systems with *ab initio* level of accuracy at much reduced computational cost. When integrated with MetaD or OPES, NNP allows us to simulate a system for the timescale of nanoseconds required to observe multiple barrier re-crossing events, which was otherwise very difficult to obtain using standard *ab initio* models. In studying the nucleation process, NNP-based ES simulations provide multiple nucleation events which allow us to calculate the underlying free energy surface.

In this work, we study the nucleation of a prototypical nanocluster, $Ag_6(SCNH_2)_6$ in methanol solvent. To enhance the efficiency of computational modeling, a smaller ligand (S-CH=NH) was used instead of the one employed in the experiment.[50] This simplification was justified by the observation that the removal of the non-functional part of the ligand

has minimal impact on the nucleation process. The selection of M_6 (M = metal) nuclearity was motivated by its compact size and its role as a critical intermediate frequently observed during the early stages of nanocluster synthesis.[20,22] It also serves as the basic building units in high-nuclearity gold clusters such as $Au_{20}(SR)_{16}$, $Au_{25}(SR)_{18}{}^{-1}$, $Au_{28}(SR)_{20}$, and $Au_{36}(SR)_{24}$, etc.[20,22,23] Notably, Luo et al.[20] proposed a mechanism for the formation of $Au_{11}(SR)_9$—an intermediate in the synthesis of $Au_{25}(SR)_{18}{}^{-1}$—via the reduction of $Au_6(SR)_6$ in the presence of carbon monoxide (CO). Furthermore, recent studies have increasingly focused on the synthesis of low-nuclearity complexes due to their enhanced properties and diverse applications.[51–56]

Using NNP-based MD and ES simulations, we investigated the dynamics of nanoclusters in solution, calculated the free energy landscape associated with the nucleation process, and simulated the spontaneous formation of multiple nanoclusters in methanol solution.

To train DNN potentials, we utilized the Deep Potential Molecular Dynamics (DeepMD) method.[57,58] The training dataset was generated through a combination of single-point density functional theory (DFT) calculations and *ab initio* molecular dynamics (AIMD) simulations, both performed using CP2K software.[59] DFT calculations employed the PBE-D3 functional[60] for exchange-correlation effects, Goedecker-Teter-Hutter (GTH) pseudopotentials to model core electrons, and a double-ζ valence basis set (DZVP) for valence electrons. The initial training data were extracted from AIMD simulations conducted in a canonical (NVT) ensemble at temperatures ranging from 300 to 450 K. This dataset was iteratively expanded by incorporating single-point calculations derived from NNP-based MD and WT-MetaD[61] simulations. Over the course of 8–10 iterations, this approach ensured a comprehensive and diverse training set, capturing the relevant configurations and interactions required for accurate potential. We validated our potential in unseen configurations, achieving excellent accuracy with RMSEs of $\sim$ 0.3 meV/atom for energies and $\sim$ 50 meV/Å for forces. Further details of the system, DFT calculations, DNN potential training and validation, and NNP-based MD simulation are given in the supporting information.

We carried out a 25 ns unbiased simulation of $Ag_6(SCNH_2)_6$ in methanol (Figure 1a,b) to evaluate the robustness of our neural network potential (NNP). From the simulation trajectory, we analyzed the distances between Ag-Ag, Ag-S, and Ag-N and obtained the probability density maxima for these distances using kernel density estimation (KDE) at 2.97 Å, 2.54 Å, and 2.28 Å, respectively (Figure 1c-e, blue curve). These values were compared with the data from the reference crystal structures of $Ag_6(SR)_6$ from two studies, labeled as exp_1[50] and exp_2.[62] In the crystal structure of $Ag_6(SR)_6$, the silver atoms adopt a distorted octahedral arrangement rather than a perfect octahedral symmetry, resulting in variations in distances and angles among Ag, S, and N atoms. Therefore, the reference values are represented as ranges, depicted by red dotted lines for exp_1 and gray dotted lines for exp_2. The simulated distances align well with the reference crystal structures. A slight deviation is observed for the Ag-S distance, where the maximum lies at the upper end of the reference range (Figure 1d). Similarly, we analyzed various angles, with probability density maxima for Ag-Ag-Ag, S-Ag-S, $(N\text{-}Ag\text{-}Ag)_1$, $(N\text{-}Ag\text{-}Ag)_2$, and N-Ag-S angles found to be 59°, 126°, 81°, 138°, and 100°, respectively. These values are generally consistent with the reference ranges, although the (N-Ag-Ag) angle exhibits a slight deviation. The deviations in distances and angles are not quite unexpected as our simulations were conducted in the solution phase, whereas the reference values are derived from solid-state structures.

Next, we modeled the nucleation process of the $Ag_6(SCNH_2)_6$ nanocluster in methanol. The nucleation of metal nanoclusters typically proceeds through the initial formation of staple motifs, which subsequently assemble to form the complete nanocluster.[20] Similarly, the nucleation of this nanocluster can be conceptualized as a two-step process. In step 1, monomeric units combine to form a dimeric staple motif. In step 2, these dimeric staple motifs aggregate in a specific orientation, forming a complete nanocluster with an octahedral silver core, as illustrated in Figure 2. The formation of dimeric staple motifs during the nucleation of hexanuclear silver clusters was recently observed experimentally by Yao and coworkers.[56] Here we have modeled both steps separately, which have been discussed in detail

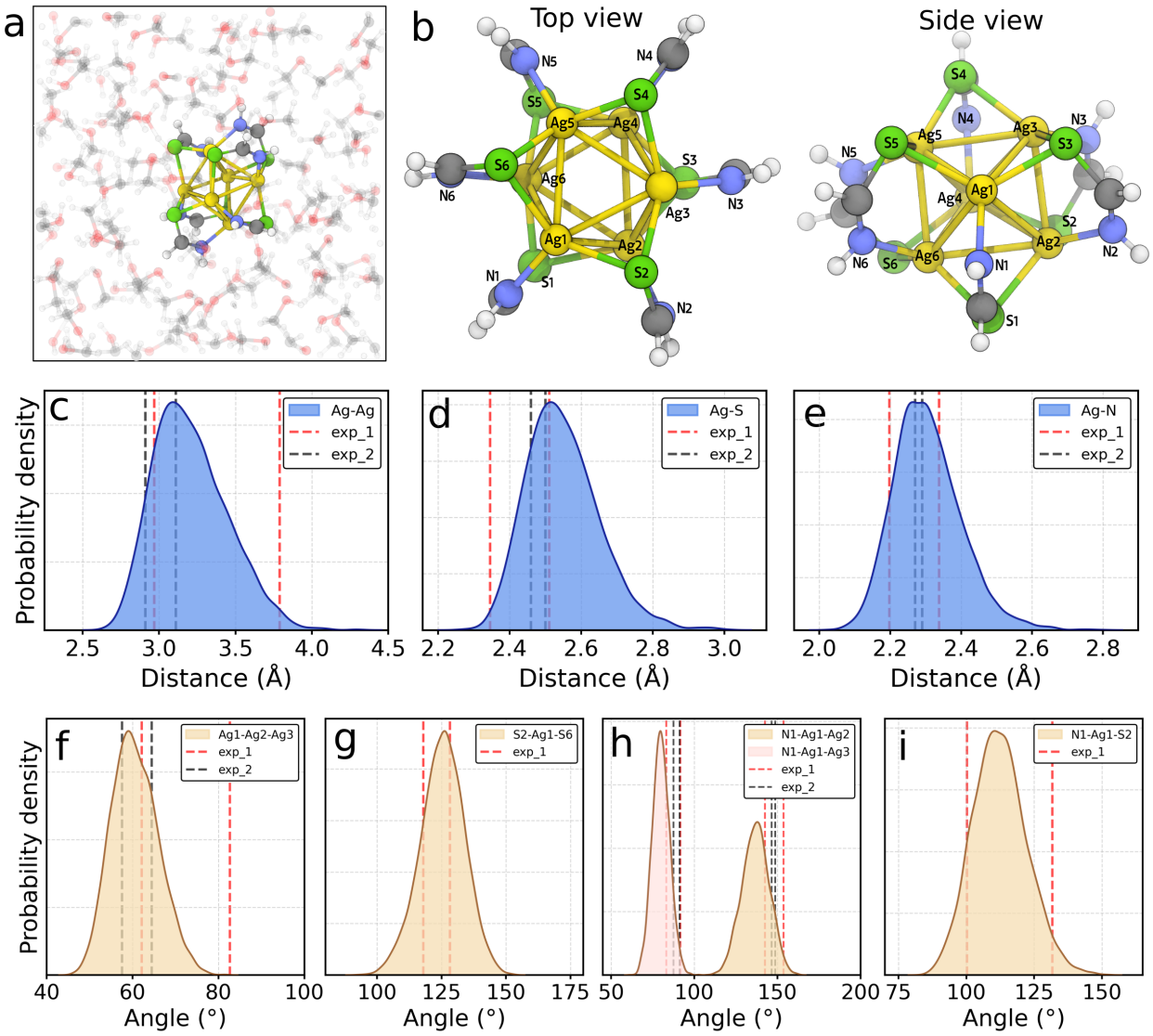

Figure 1: (a) Representation of the system comprising an $Ag_6(SCNH_2)_6$ nanocluster and 150 methanol molecules within a cubic box of 20 Å length. (b) Top (left) and side (right) views of the $Ag_6(SCNH_2)_6$ nanocluster, with silver, sulfur, and nitrogen atoms labeled. Kernel density estimation (KDE) plots for distances: (c) Ag-Ag, (d) Ag-S, and (e) Ag-N, and for angles: (f) Ag-Ag-Ag, (g) S-Ag-S, (h) N-Ag-Ag, and (i) N-Ag-S.Color code for atoms: Ag (yellow), S (green), N (blue), O (red), C (gray), and H (white).

in subsequent sections.

To investigate the monomer-to-dimer transitions, we developed an NNP for a system containing two monomeric units and 120 methanol molecules. We carried out a Well-Tempered Metadynamics (WTMetaD) simulation using two collective variables (CVs): s_1, defined as the solute coordination number, which combines the Ag-Ag and Ag-N coordination; and s_2,

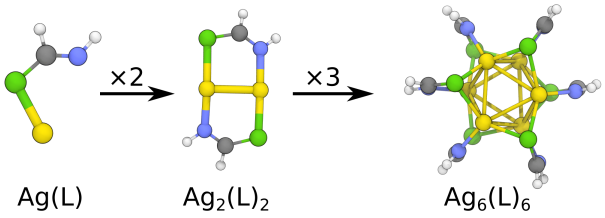

Figure 2: Illustration of formation mechanism of $Ag_6(SCNH_2)_6$ nanocluster.

representing the number of solvent molecules coordinated with the center of mass (COM) of the silver atoms (see Section 4.2 of ESI for further details). Multiple back-and-forth transitions were observed between the monomeric (D) and dimeric (A) states within 4.5 ns of the WTMetaD simulation (Figure 3a). The reweighted free energy surface (FES) was calculated and plotted as a function of s_1 and s_2 (Figure 3b). The convergence of FES was confirmed by two methods: (i) plotting the block-averaged FES with associated errors along s_1 (Figure S4a) and (ii) tracking the free energy difference (ΔG) over the simulation time (Figure S4b). The distinct states, marked as A, B, C, and D, observed in the FES, were classified based on the number and coordination mode of the solvent molecules (Figure 3c).

The dimerization free energy surface indicates an almost barrierless transition from the monomeric dispersed state **D** to the dimeric state **A**, indicating the facile formation of dimeric staple units from the monomers. The dimeric state **A** is stable by $\sim$ 30 kcal/mol compared to the monomeric **D** unit. Interestingly, in the state **D**, the H1 proton interacting with N1 nitrogen often shuttles between the oxygen of methanol and the nitrogen of the nanocluster, leading to protonated (N-H $\sim$ 1.0 Å) and deprotonated (N-H $\sim$ 1.5 Å) ligand states (Figure S5c, blue curve). The number of solvents gradually decreases from state D to C, in which two methanol molecules hold the two MPC monomeric units. Here, at each end, the methanol proton (H1) interacts with N1 ($d_{N1-H1} \sim$ 1.5 Å), while oxygen (O1) interacts with Ag1 ($d_{Ag1-O1} \sim$ 2.5 Å) (Figure S5a), keeping the two MPC monomers separated by solvent molecules. In state B, one methanol remains bridged between the MPC units. Finally, the dimeric state A is formed when the two MPC units attach by fully removing the solvent molecules. The transition from monomers to a dimer has been monitored by calculating the

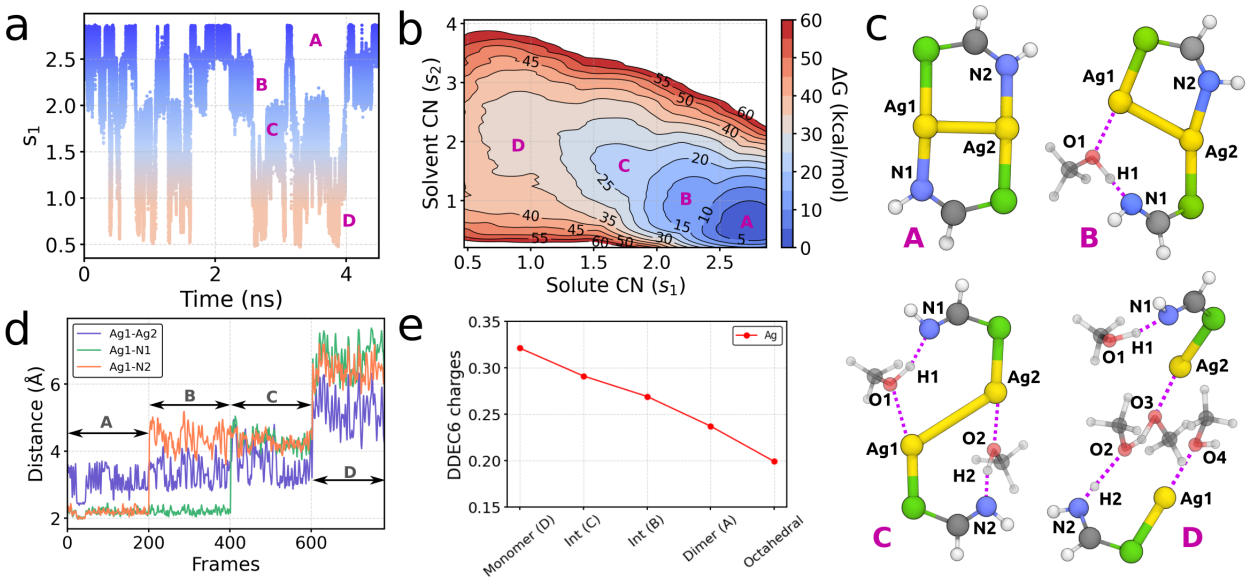

Figure 3: (a) Time evolution of collective variable (s_1) for monomer-dimer transition, (b) free energy profile as a function of s_1 and s_2, (c) representative structures of intermediates from free energy surface (FES), (d) Ag-Ag and Ag-N distance evolution along the representative structures from different states, (e) variation in partial atomic charge calculated using DDEC6 analysis on silver (Ag) atoms in different states from monomer to octahedral.

distances Ag1-Ag2, Ag1-N1, and Ag2-N2 (Figure 3d). The Ag1-Ag2 distance in structures A, B, and C remains similar ($\sim$ 3.0 Å), while the distance increases beyond 3.5 Å in the monomeric state **D**.

To further investigate the driving force for the barrierless nucleation process, we performed DDEC6 charge analysis[63,64] and calculated the charge distribution in the monomeric and dimeric states (Table S3). This analysis revealed a systematic decrease in the charge of silver atoms as the system transitions from the monomeric to the dimeric state (Figure 3e). This reduction in charge is mainly attributed to the change in the interaction partners, moving from the more electronegative oxygen atoms of the methanol solvent to the less electronegative nitrogen atoms of the ligand. In contrast, the charges on the sulfur and nitrogen atoms remained relatively unchanged throughout the transition (Figure S1b). An interplay between the charges on solutes and those in solvents mediates the early stage of MPC nucleation.

Having realized that the dimeric state is significantly more stable than the monomers,

we conjecture that the dimeric units could be the basic building blocks for nanocluster formation. Thus, in the second set of simulations, we investigated the formation of octahedral nanoclusters from the dimeric staple motifs. With an NNP, we carried out WTMetaD simulations with two CVs: s_3 and s_4. The first CV, s_3, is the sum of the coordination number of Ag atoms with the nucleation point (c) and Ag atoms with S atoms. The nucleation point is located near the center of the simulation box. To maintain the system's proximity to this point, we applied a restraint to the center of mass (COM) of the Ag atoms, ensuring it remained near the nucleation point throughout the process. The second CV, s_4 is the number of solvents coordinated around the nucleation point (see Section 4.2 of ESI for further details).

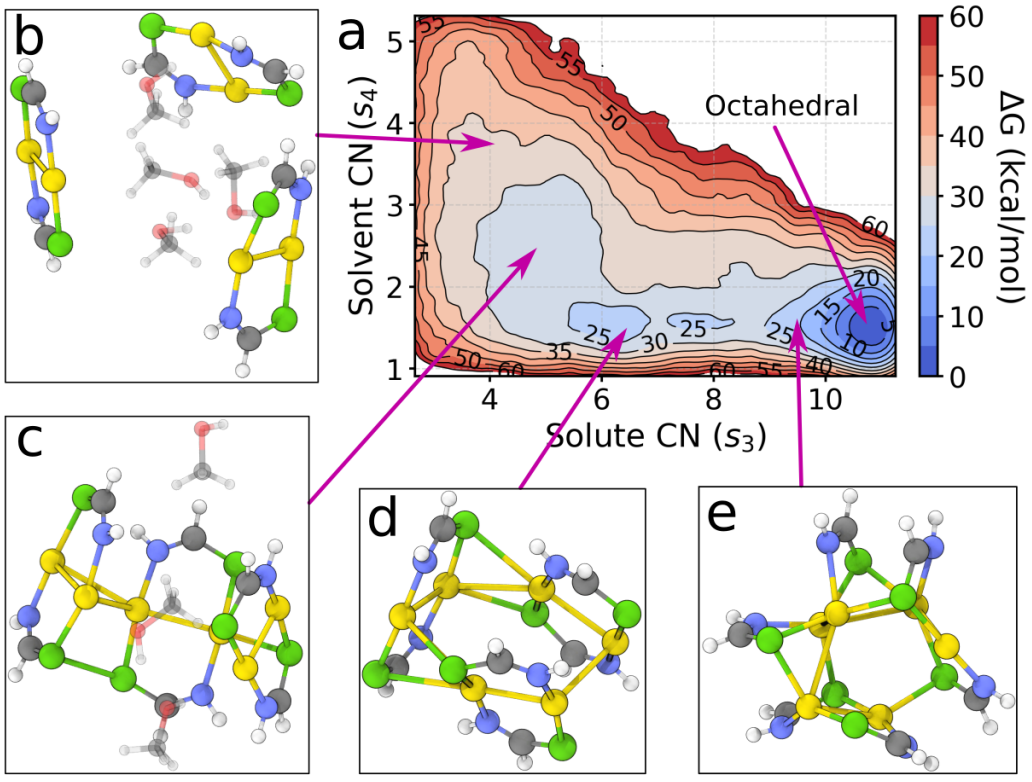

Figure 4: (a) Free energy profile as a function of s_3 and s_4 along with the representative structures from different regions of the FES [(b), (c), (d) and (e)]

The free energy surface (FES) was calculated using the same protocol as that of the monomer-dimer case and plotted as a function of s_3 and s_4 (Figure 4). The FES shows a

downhill nucleation process. Unlike the monomer-to-dimer transition, the lowest free energy path for the dimer-to-octahedral transition is not diagonal. Instead, it follows an L-shaped landscape from the dispersed dimer state to the nucleated octahedral state (Figure 4). The first step involves the removal of solvent molecules from the nucleation point, referred to as the "drying step". This step facilitates the aggregation of dimers to form an intermediate state, which in the subsequent "reorganization step", undergoes a reorganization in a specific orientation, resulting in the formation of the perfect octahedral nanocluster. This stepwise nucleation closely resembles the standard two-step nucleation mechanism in atomic and molecular crystals.[65]

The facile generation of dimers from MPC monomeric units followed by their aggregation leading to the formation of an octahedral nanocluster motivated us to investigate whether we could simulate the spontaneous nucleation of nanoclusters. We prepared a system consisting of a cubic box with a 5 nm edge length, containing 30 randomly dispersed dimer motifs in methanol (Figure 5a).

Within 350 ps of simulation using an NNP model, two perfectly nucleated nanoclusters (labeled C* and D* in Figure 5b, Video S1) were observed along with other aggregated structures (Figure 5c). We analyzed the time evolution of the Ag-Ag coordination number (Figure 5d, top) to monitor the nucleation process. A stepwise increase in Ag-Ag coordination was observed, indicating different stages in the nucleation process. The first steep rise (A) corresponds to the aggregation of multiple dimers. Around 100 ps, several dimers aggregate in a larger intermediate state **B** (Figure 5c, left). By approximately 180 ps, we observed the formation of nanocluster C* and shortly afterward, around 220 ps, nanocluster D*. Subsequently, another group of three dimers led to the formation of a slightly disordered nucleus **E** (Figure 5c, right). To further investigate the mechanism of nanocluster formation, we analyzed the time evolution of coordination numbers around the nucleation point (Figure 5e). Specifically, we analyzed the coordination number of Ag atoms near the nucleation point (Figure 5d, middle) and the coordination number of solvent molecules surrounding

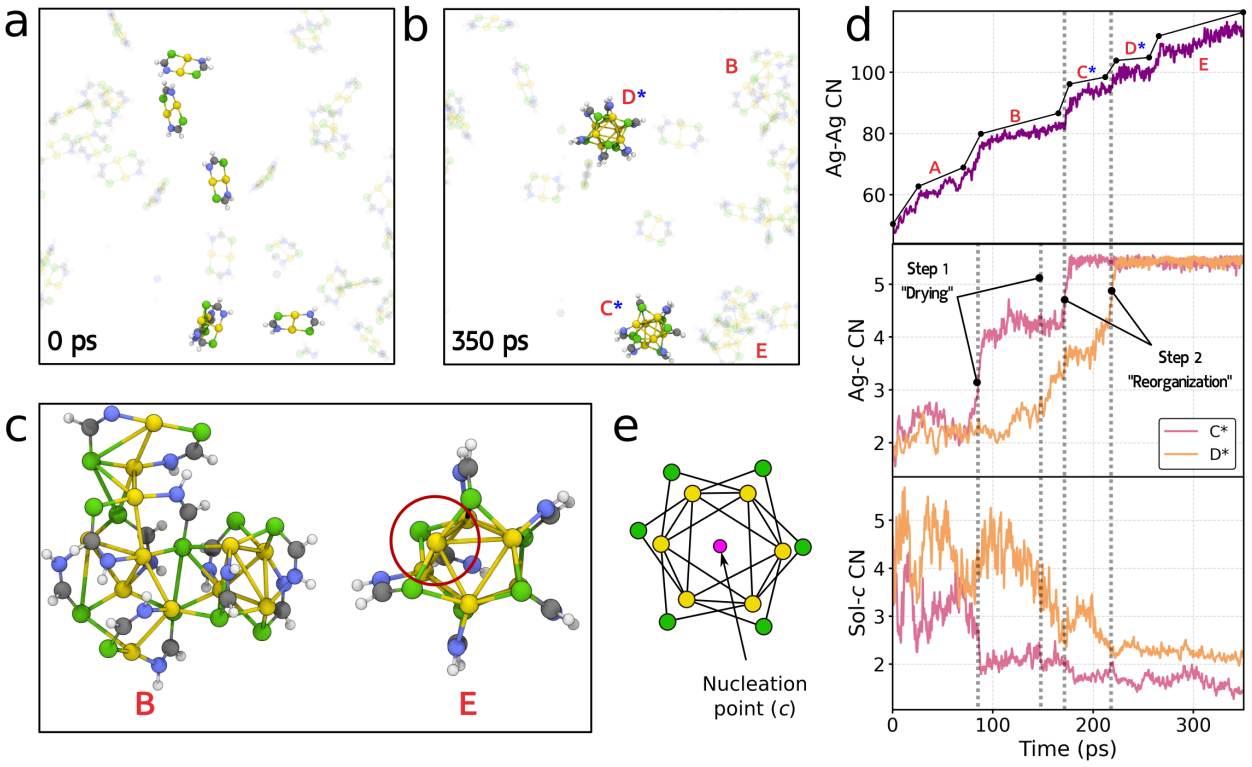

Figure 5: Spontaneous nucleation from 30 dispersed dimeric staple motifs in methanol. (a) Initial dispersed state of the motifs, (b) final nucleated state displaying two perfectly formed nuclei (C* and D*) alongside partially aggregated states (B and E), (c) structural representations of aggregates B (left) and E (right), (d) time evolution graph illustrating changes in Ag-Ag coordination number (top), Ag-c coordination number (middle), and solvent-c coordination number (bottom), (e) schematic representation of the nucleation point (c) defined as the center of mass (COM) of Ag atoms.

the nucleation point (Figure 5d, bottom). These analyses highlight the two distinct steps of nanocluster formation: "drying" and 'reorganization' as discussed earlier. This simulation of spontaneous nucleation further supports the previously discussed two-step nucleation mechanism, where aggregation and reorganization occur as distinct steps in the formation of nanoclusters.

This study elucidates the nucleation mechanism of $Ag_6(SCNH_2)_6$ nanoclusters in methanol, highlighting a two-step process involving intermediate aggregation followed by structural reorganization into an octahedral nanocluster. Both monomer-to-dimer and dimer-octahedral transitions were nearly barrierless, underscoring the ease of forming stable nanoclusters.

The dimer-to-octahedral transition follows a L-shaped free energy path, which emphasizes solvent removal as the initial “drying step" followed by reorganization into the final structure. Furthermore, spontaneous nucleation simulations confirm the aggregation of dimers into intermediates and their transformation into ordered nuclei, providing dynamic insights into the nucleation process. Our findings align with the two-step nucleation model, where intermediate states play a critical role in cluster formation. This work enhances our understanding of metal-ligand nanocluster formation and offers a framework for studying similar mechanisms in other nanostructured systems.

Data availability

All input files required to run the simulations presented in this work can be found in a public GitHub repository (https://github.com/vikast282/Ag6L6_nucleation) and PLUMED-NEST[?] (ID:).

Acknowledgement

VT thanks the Ministry of Education, Govt. of India, for the PMR Fellowship. TK acknowledges the Science and Engineering Research Board (SERB), New Delhi, India, for the Start-up Research Grant (File No. SRG/2022/000969). We also acknowledge IIT Delhi for the Seed Grant and thank the IIT Delhi HPC facility for computational resources.

Supporting Information Available

The following files are available free of charge.

- Supporting information.pdf: This file contains details of the systems simulated, NN data, NNP validation, WT-Metad simulation parameters, and collective variables.

- Video_S1.mp4: Spontaneous formation of multiple nucleated nanoclusters.

References

(1) Chakraborty, I.; Pradeep, T. Atomically precise clusters of noble metals: emerging link between atoms and nanoparticles. *Chemical reviews* **2017**, *117*, 8208–8271.

(2) Jin, R.; Zeng, C.; Zhou, M.; Chen, Y. Atomically precise colloidal metal nanoclusters and nanoparticles: fundamentals and opportunities. *Chemical reviews* **2016**, *116*, 10346–10413.

(3) Li, S.; Li, N.-N.; Dong, X.-Y.; Zang, S.-Q.; Mak, T. C. Chemical Flexibility of Atomically Precise Metal Clusters. *Chemical Reviews* **2024**, *124*, 7262–7378.

(4) Du, X.; Jin, R. Atomically precise metal nanoclusters for catalysis. *Acs Nano* **2019**, *13*, 7383–7387.

(5) Du, Y.; Sheng, H.; Astruc, D.; Zhu, M. Atomically precise noble metal nanoclusters as efficient catalysts: a bridge between structure and properties. *Chemical reviews* **2019**, *120*, 526–622.

(6) Higaki, T.; Li, Y.; Zhao, S.; Li, Q.; Li, S.; Du, X.-S.; Yang, S.; Chai, J.; Jin, R. Atomically tailored gold nanoclusters for catalytic application. *Angewandte Chemie* **2019**, *131*, 8377–8388.

(7) Ahmad, M.; Nawaz, T.; Eddahani, Y.; Hussain, I.; Chen, X.; Low, K. H.; He, J.; Zhang, K. Strategic Fabrication of Au4Cu2 NC/ZIF-8 Composite Via In Situ Integration Technique for Enhanced Energy Storage Applications. *Advanced Functional Materials* **2024**, *34*, 2407059.

(8) Munir, A.; Joya, K. S.; Ul Haq, T.; Babar, N.-U.-A.; Hussain, S. Z.; Qurashi, A.;

Ullah, N.; Hussain, I. Metal nanoclusters: new paradigm in catalysis for water splitting, solar and chemical energy conversion. *ChemSusChem* **2019**, *12*, 1517–1548.

(9) Wang, Y.; Cui, X.; Zhang, J.; Qiao, J.; Huang, H.; Shi, J.; Wang, G. Advances of atomically dispersed catalysts from single-atom to clusters in energy storage and conversion applications. *Progress in Materials Science* **2022**, *128*, 100964.

(10) Ou, G.; Zhao, J.; Chen, P.; Xiong, C.; Dong, F.; Li, B.; Feng, X. Fabrication and application of noble metal nanoclusters as optical sensors for toxic metal ions. *Analytical and bioanalytical chemistry* **2018**, *410*, 2485–2498.

(11) Zhang, L.; Wang, E. Metal nanoclusters: new fluorescent probes for sensors and bioimaging. *Nano Today* **2014**, *9*, 132–157.

(12) Sun, J.; Jin, Y. Fluorescent Au nanoclusters: recent progress and sensing applications. *Journal of Materials Chemistry C* **2014**, *2*, 8000–8011.

(13) Tao, Y.; Li, M.; Ren, J.; Qu, X. Metal nanoclusters: novel probes for diagnostic and therapeutic applications. *Chemical Society Reviews* **2015**, *44*, 8636–8663.

(14) van de Looij, S. M.; Hebels, E. R.; Viola, M.; Hembury, M.; Oliveira, S.; Vermonden, T. Gold nanoclusters: imaging, therapy, and theranostic roles in biomedical applications. *Bioconjugate Chemistry* **2021**, *33*, 4–23.

(15) An, Y.; Ren, Y.; Bick, M.; Dudek, A.; Waworuntu, E. H.-W.; Tang, J.; Chen, J.; Chang, B. Highly fluorescent copper nanoclusters for sensing and bioimaging. *Biosensors and Bioelectronics* **2020**, *154*, 112078.

(16) Hossain, S.; Hirayama, D.; Ikeda, A.; Ishimi, M.; Funaki, S.; Samanta, A.; Kawawaki, T.; Negishi, Y. Atomically precise thiolate-protected gold nanoclusters: Current status of designability of the structure and physicochemical properties. *Aggregate* **2023**, *4*, e255.

(17) Goswami, N.; Yao, Q.; Chen, T.; Xie, J. Mechanistic exploration and controlled synthesis of precise thiolate-gold nanoclusters. *Coordination Chemistry Reviews* **2016**, *329*, 1–15.

(18) Matus, M. F.; Häkkinen, H. Understanding ligand-protected noble metal nanoclusters at work. *Nature Reviews Materials* **2023**, *8*, 372–389.

(19) Li, Q.; Pan, Y.; Chen, T.; Du, Y.; Ge, H.; Zhang, B.; Xie, J.; Yu, H.; Zhu, M. Design and mechanistic study of a novel gold nanocluster-based drug delivery system. *Nanoscale* **2018**, *10*, 10166–10172.

(20) Luo, Z.; Nachammai, V.; Zhang, B.; Yan, N.; Leong, D. T.; Jiang, D.-e.; Xie, J. Toward understanding the growth mechanism: tracing all stable intermediate species from reduction of Au (I)–thiolate complexes to evolution of Au25 nanoclusters. *Journal of the American Chemical Society* **2014**, *136*, 10577–10580.

(21) Luo, X.-M.; Huang, S.; Luo, P.; Ma, K.; Wang, Z.-Y.; Dong, X.-Y.; Zang, S.-Q. Snapshots of key intermediates unveiling the growth from silver ions to Ag70 nanoclusters. *Chemical Science* **2022**, *13*, 11110–11118.

(22) Chai, O. J. H.; Xie, J. Unraveling the Mechanism of the Brust-Schiffrin Formation of Au25 (SR) 18 through Mass Spectrometry. *The Journal of Physical Chemistry Letters* **2024**, *15*, 5137–5142.

(23) Liu, C.; Pei, Y.; Sun, H.; Ma, J. The nucleation and growth mechanism of thiolate-protected Au nanoclusters. *Journal of the American Chemical Society* **2015**, *137*, 15809–15816.

(24) Xiong, L.; Pei, Y. Symmetric Growth of Dual-Packed Kernel: Exploration of the Evolution of Au40 (SR) 24 to Au49 (SR) 27 and Au58 (SR) 30 Clusters via the 2 e—Reduction Cluster Growth Mechanism. *ACS omega* **2021**, *6*, 18024–18032.

(25) Wang, P.; Peng, J.; Pei, Y. An Au2S network model for exploring the structural origin, evolution, and two-electron (2e-) reduction growth mechanism of Aun (SR) m clusters. *The Journal of Chemical Physics* **2021**, *154*.

(26) van Der Linden, M.; van Bunningen, A. J.; Delgado-Jaime, M. U.; Detlefs, B.; Glatzel, P.; Longo, A.; de Groot, F. M. Insights into the synthesis mechanism of Ag29 nanoclusters. *The Journal of Physical Chemistry C* **2018**, *122*, 28351–28361.

(27) Finney, E. E.; Finke, R. G. Nanocluster nucleation and growth kinetic and mechanistic studies: A review emphasizing transition-metal nanoclusters. *Journal of Colloid and Interface Science* **2008**, *317*, 351–374.

(28) Tang, Q.; Hu, G.; Fung, V.; Jiang, D.-e. Insights into interfaces, stability, electronic properties, and catalytic activities of atomically precise metal nanoclusters from first principles. *Accounts of chemical research* **2018**, *51*, 2793–2802.

(29) Nair, A. S.; Pathak, B. Computational strategies to address the catalytic activity of nanoclusters. *Wiley Interdisciplinary Reviews: Computational Molecular Science* **2021**, *11*, e1508.

(30) Malola, S.; Häkkinen, H. Prospects and challenges for computer simulations of monolayer-protected metal clusters. *Nature Communications* **2021**, *12*, 2197.

(31) Jäger, M. O.; Morooka, E. V.; Federici Canova, F.; Himanen, L.; Foster, A. S. Machine learning hydrogen adsorption on nanoclusters through structural descriptors. *npj Computational Materials* **2018**, *4*, 37.

(32) Jager, M. O.; Ranawat, Y. S.; Canova, F. F.; Morooka, E. V.; Foster, A. S. Efficient machine-learning-aided screening of hydrogen adsorption on bimetallic nanoclusters. *ACS combinatorial science* **2020**, *22*, 768–781.

(33) Panapitiya, G.; Avendaño-Franco, G.; Ren, P.; Wen, X.; Li, Y.; Lewis, J. P. Machine-learning prediction of CO adsorption in thiolated, Ag-alloyed Au nanoclusters. *Journal of the American Chemical Society* **2018**, *140*, 17508–17514.

(34) Mastracco, P.; Gonzàlez-Rosell, A.; Evans, J.; Bogdanov, P.; Copp, S. M. Chemistry-informed machine learning enables discovery of DNA-stabilized silver nanoclusters with near-infrared fluorescence. *ACS nano* **2022**, *16*, 16322–16331.

(35) Mastracco, P.; Copp, S. M. Beyond nature's base pairs: machine learning-enabled design of DNA-stabilized silver nanoclusters. *Chemical Communications* **2023**, *59*, 10360–10375.

(36) Tang, L.; Wang, L.; Wang, B.; Pei, Y.; Wang, S. Discovering Syntheses of Atomically Precise Metal Nanoclusters by Applying Machine Learning to a High-Throughput Platform. *Chemistry–A European Journal* **2024**, e202302602.

(37) Ghosh, A.; Datta, S.; Saha-Dasgupta, T. Understanding the trend in core–shell preferences for bimetallic nanoclusters: A machine learning approach. *The Journal of Physical Chemistry C* **2022**, *126*, 6847–6853.

(38) Zeni, C.; Rossi, K.; Glielmo, A.; Fekete, Á.; Gaston, N.; Baletto, F.; De Vita, A. Building machine learning force fields for nanoclusters. *The Journal of chemical physics* **2018**, *148*.

(39) Bharadwaj, N.; Roy, D.; Das, A.; Pathak, B. Machine Learning-Driven Screening of Atomically Precise Pure Metal Nanoclusters for Oxygen Reduction. *ACS Materials Letters* **2025**, *7*, 500–507.

(40) Pihlajamaki, A.; Hamalainen, J.; Linja, J.; Nieminen, P.; Malola, S.; Karkkainen, T.; Hakkinen, H. Monte Carlo simulations of Au38 (SCH3) 24 nanocluster using distance-based machine learning methods. *The Journal of Physical Chemistry A* **2020**, *124*, 4827–4836.

(41) Wang, S.; Wu, Z.; Dai, S.; Jiang, D.-e. Deep learning accelerated determination of hydride locations in metal nanoclusters. *Angewandte Chemie* **2021**, *133*, 12397–12400.

(42) McCandler, C. A.; Pihlajamaki, A.; Malola, S.; Hakkinen, H.; Persson, K. A. Gold–Thiolate Nanocluster Dynamics and Intercluster Reactions Enabled by a Machine Learned Interatomic Potential. *ACS nano* **2024**, *18*, 19014–19023.

(43) Banik, S.; Dutta, P. S.; Manna, S.; Sankaranarayanan, S. K. Development of a Machine Learning Potential to Study the Structure and Thermodynamics of Nickel Nanoclusters. *The Journal of Physical Chemistry A* **2024**, *128*, 10259–10271.

(44) Perego, S.; Bonati, L.; Tripathi, S.; Parrinello, M. How dynamics changes ammonia cracking on iron surfaces. *ACS Catalysis* **2024**, *14*, 14652–14664.

(45) Tripathi, S.; Bonati, L.; Perego, S.; Parrinello, M. How Poisoning Is Avoided in a Step of Relevance to the Haber–Bosch Catalysis. *ACS Catalysis* **2024**, *14*, 4944–4950.

(46) Gardini, A. T.; Raucci, U.; Parrinello, M. A Bulk Phase Transformation Drives Ammonia Synthesis on Barium Hydride. **2024**,

(47) Anmol; Karmakar, T. Unveiling the Role of Solvent in Solution Phase Chemical Reactions using Deep Potential-Based Enhanced Sampling Simulations. *The Journal of Physical Chemistry Letters* **2024**, *15*, 9932–9938.

(48) Gomez, A.; Thompson, W. H.; Laage, D. Neural-network-based molecular dynamics simulations reveal that proton transport in water is doubly gated by sequential hydrogen-bond exchange. *Nature Chemistry* **2024**, *16*, 1838–1844.

(49) Benayad, Z.; David, R.; Stirnemann, G. Prebiotic chemical reactivity in solution with quantum accuracy and microsecond sampling using neural network potentials. *Proceedings of the National Academy of Sciences* **2024**, *121*, e2322040121.

(50) Wu, Y.; Wu, X.; Fang, S.; Yang, S.; Li, W.; Wang, H.; Yu, X. A novel hexanuclear silver (I) complex with photoluminescence properties. *Polyhedron* **2017**, *122*, 155–160.

(51) Gu, J.; Xu, Y.; Lu, J. Atom-precise low-nuclearity cluster catalysis: Opportunities and challenges. *Acs Catalysis* **2023**, *13*, 5609–5634.

(52) Devi, A.; Minhas, H.; Sahoo, L.; Gratious, S.; Das, A.; Mandal, S.; Pathak, B.; Patra, A.; others Insights of the efficient hydrogen evolution reaction performance in bimetallic Au 4 Cu 2 nanoclusters. *Nanoscale* **2024**, *16*, 1758–1769.

(53) Chen, Y.-T.; Krytchankou, I. S.; Karttunen, A. J.; Grachova, E. V.; Tunik, S. P.; Chou, P.-T.; Koshevoy, I. O. Silver alkynyl-phosphine clusters: an electronic effect of the alkynes defines structural diversity. *Organometallics* **2017**, *36*, 480–489.

(54) Chen, H.; Zhang, X.; Fu, K.; Wang, X.; Liu, G. Ligand engineering of circularly polarized luminescence inversion and enhancement for chiral Ag 6 nanoclusters. *Journal of Materials Chemistry C* **2024**, *12*, 8287–8295.

(55) Tseng, Y.-M.; Liao, J.-H.; Chiu, T.-H.; Liang, H.; Kahlal, S.; Saillard, J.-Y.; Liu, C. Superatom Pruning by Diphosphine Ligands as a Chemical Scissor. *Inorganic Chemistry* **2023**, *62*, 3866–3874.

(56) Xiang, H.; Wang, Y.; Xu, X.; Ruan, C.; Wang, K.; Cheng, W.; Zhou, M.; Liu, X.; Yao, C. Reversible interconversion between Ag2 and Ag6 clusters and their responsive optical properties. *Journal of the American Chemical Society* **2024**, *146*, 28572–28579.

(57) Zhang, L.; Han, J.; Wang, H.; Car, R.; E, W. Deep potential molecular dynamics: a scalable model with the accuracy of quantum mechanics. *Physical review letters* **2018**, *120*, 143001.

(58) Zeng, J.; Zhang, D.; Lu, D.; Mo, P.; Li, Z.; Chen, Y.; Rynik, M.; Huang, L.; Li, Z.;

Shi, S.; others DeePMD-kit v2: A software package for deep potential models. *The Journal of Chemical Physics* **2023**, *159*.

(59) Kühne, T. D.; Iannuzzi, M.; Del Ben, M.; Rybkin, V. V.; Seewald, P.; Stein, F.; Laino, T.; Khaliullin, R. Z.; Schütt, O.; Schiffmann, F.; others CP2K: An electronic structure and molecular dynamics software package-Quickstep: Efficient and accurate electronic structure calculations. *The Journal of Chemical Physics* **2020**, *152*.

(60) Perdew, J. P.; Burke, K.; Ernzerhof, M. Generalized gradient approximation made simple. *Physical review letters* **1996**, *77*, 3865.

(61) Barducci, A.; Bussi, G.; Parrinello, M. Well-tempered metadynamics: a smoothly converging and tunable free-energy method. *Physical review letters* **2008**, *100*, 020603.

(62) Nomiya, K.; Takahashi, S.; Noguchi, R. Synthesis and crystal structure of a hexanuclear silver (I) cluster [Ag (Hmna)] 6· 4H 2 O (H 2 mna= 2-mercaptonicotinic acid) and a supramolecular gold (I) complex H [Au (Hmna) 2] in the solid state, and their antimicrobial activities. *Journal of the Chemical Society, Dalton Transactions* **2000**, 2091–2097.

(63) Manz, T. A.; Limas, N. G. Introducing DDEC6 atomic population analysis: part 1. Charge partitioning theory and methodology. *RSC advances* **2016**, *6*, 47771–47801.

(64) Limas, N. G.; Manz, T. A. Introducing DDEC6 atomic population analysis: part 2. Computed results for a wide range of periodic and nonperiodic materials. *RSC advances* **2016**, *6*, 45727–45747.

(65) Erdemir, D.; Lee, A. Y.; Myerson, A. S. Nucleation of crystals from solution: classical and two-step models. *Accounts of chemical research* **2009**, *42*, 621–629.